Pushing the Energy Output and Cyclability of Sodium Hybrid Capacitors at High Power to New Limits

*Ranjith Thangavel, Brindha Moorthy, Do Kyung Kim, and Yun-Sung Lee**

Hybrid capacitors, especially sodium hybrid capacitors (NHCs), have continued to gain importance and are extensively studied based on their excellent potential to serve as advanced devices for fulfilling high energy and high power requirements at a low cost. To achieve remarkable performance in hybrid capacitors, the two electrodes employed must be superior with enhanced charge storage capability and fast kinetics. In this study, a new sodium hybrid capacitor system with a sodium super ionic conductor $NaTi_2(PO_4)_3$ grown on graphene nanosheets as an intercalation electrode and 2D graphene nanosheets as an adsorption electrode is reported for the first time. This new system delivers a high energy density of ≈80 W h kg^{-1} and a high specific power of 8 kW kg^{-1}. An ultralow performance fading of ≈0.13% per 1000 cycles (90%–75 000 cycles) outperforms previously reported sodium ion capacitors. The enhanced charge transfer kinetics and reduced interfacial resistance at high current rates deliver a high specific energy without compromising the high specific power along with high durability, and thereby bridge batteries and capacitors. This new research on kinetically enhanced NHCs can be a trendsetter for the development of advanced energy storage devices requiring high energy—high power.

1. Introduction

The increasing demand for energy in day-to-day life has triggered immense interest in energy storage devices as a means of delivering the required energy.[1–4] The domain of energy storage devices ranges from portable electronic devices to large-scale electric vehicles and smart grid applications.[4–6] Intensive research have fuelled a tremendous change in battery technology from the traditional primary Daniel cell to modern high energy rechargeable lithium ion batteries.[5,7] Simultaneously, the increase in the demand for lithium batteries has propelled an upsurge in the price of lithium resources over the past decades.[8,9] This has necessitated the replacement of lithium with widely available and low cost sodium resources as an alternative in the energy storage devices.[5,10] Given the similar chemistry and almost equivalent energy density as lithium analogs, sodium ion batteries are almost on the verge of commercialization and investigation is still underway to make them widely available for many applications.[10–12] Regardless of the change, batteries have failed to satisfy consumer needs in many aspects, especially in terms of next-generation high power applications.[13] The emerging high power devices can neither be powered by state-of-the-art lithium ion batteries nor by low cost sodium ion batteries due to the limited power of such batteries, driven by slow intercalation and deintercalation kinetics.[7,14,15] Although high power electrochemical double layer capacitors (EDLCs) can supply the requisite power, they are inferior to batteries in supplying the necessary energy density.[7,13,16–19]

Hybrid capacitors (HCs) are a new class of energy storage device that bridge the gap between batteries and EDLCs by delivering high energy at high power without sacrificing the stability, and thereby fulfilling the needs of high power applications.[20,21] HCs operate by the following dual mechanism that occurs simultaneously in two asymmetric electrodes: (i) intercalation/deintercalation of cations delivering high energy and (ii) surface adsorption and desorption of anions supplying high power and stability. Successful intercalation/deintercalation of sodium ions into a suitable electrode paves the way for development of novel, low cost sodium hybrid capacitor systems.[22–24] Sodium hybrid capacitors with the right combination of insertion and adsorption electrodes that are kinetically well balanced can retain high energy density and power density with robust durability.[21,24–26]

Various intercalation-based electrodes, including layered oxides, sulfates, metal oxides, phosphates, fluorophosphates, hard carbons, red phosphorous, and much more, have been investigated for sodium ion batteries.[27–29] In general, sodium insertion electrodes suffer from poor sodium insertion kinetics and poor structural integrity due to the quick transition metal loss and large lattice strain that occur during sodium insertion, thereby restricting their application in hybrid capacitors. However, sodium super ionic conductor (NASICON) structured—$NaTi_2(PO_4)_3$ (NTP)—insertion materials are considered to be the best choice for hybrid capacitor application due to their high ionic conductivity, quick sodium insertion into their structure due to their ultrafast sodium ion kinetics, and structural stability.[12,30–32] Further, sodium ions can be inserted into NTP materials without compromising their structural integrity, which could further improve their energy retention for longer

R. Thangavel, Prof. Y.-S. Lee
Faculty of Applied Chemical Engineering
Chonnam National University
Gwang-ju 500-757, Republic of Korea
E-mail: leeys@chonnam.ac.kr
B. Moorthy, Prof. D. K. Kim
Department of Materials Science and Engineering
Korea Advanced Institute of Science and Engineering (KAIST)
Daejeon 305-701, Republic of Korea

DOI: 10.1002/aenm.201602654

cycles.[33] In addition, the poor intrinsic electronic conductivity of NTP can be easily overcome by using various carbon-based materials to provide quick and easy electron flow.[34,35] In particular, the use of graphene as a conductive matrix for NTP led to highly enhanced kinetics with superior sodium insertion/extraction at high current rates with ultralong stability.[35,36] Therefore, NTP grown directly on graphene nanosheets (GNTP) as an intercalation electrode would be advantageous for delivering higher energy density with faster reaction kinetics to match the power performance of the adsorption electrode.

In the case of the adsorption electrodes, highly porous carbons with high surface area that exhibit high capacitance have been widely explored. Specifically, activated carbons (AC) have been commonly used because of the facile manufacturing process.[17] Although porous carbons from various precursors have been successfully adapted in hybrid capacitors, their power density is yet to reach the satisfactory level for practical implementation in an efficient device.[20,37] The poor electronic conductivity of porous carbon undermines their performance by impeding the ion adsorption kinetics at high current condition and thereby curtailing achievement of more power.[25,37] In spite of the high porosity and large surface area, not all the pores of these carbon materials are easily accessed by ions at higher current due to the poor ion transport inside the pores, thereby limiting the kinetics and leading to disproportionate capacitance and reduced cycle life.[25] The prime issue to be addressed is the kinetic imbalance between the two electrodes that causes the entire capacitor system to collapse, with consequently poor and inferior performance.[38] The adsorption kinetics of the carbon-based electrodes must be equivalent to that of the intercalation electrode by storage of equivalent amounts of anions on the surface of the carbon-based electrode.

One approach to overcome the limitation of carbon-based electrodes is by utilizing graphene as an adsorption electrode. Graphene is attractive due its high surface area (>2600 $m^2 g^{-1}$), unique physico-chemical properties, and ultrahigh electronic conductivity. Graphene nanosheets (GNS) have been intensively studied for use in EDLCs that exhibit extraordinary power and superior cyclability due to their quick kinetics.[39,40] Unlike activated carbons, where many of the pores are not quickly accessible by ions, the surface of 2D nanosheets can be easily accessed by ions in the electrolyte, thereby reducing the ion transport distance.[14,25] With these advantages, graphene represents a promising adsorption electrode for hybrid capacitor application, where surface utilization (ultrafast surface reaction) by anions is much higher than in the case of porous carbon, making it possible to easily achieve high power. Although a variety of graphene materials with different properties, morphologies, and chemical structures have been analyzed for EDLCs, utilizing 2D material for NHCs has not been studied widely. Thus, exploration of graphene in this context can greatly improve the power density of sodium based energy storage systems, which is currently limited by the poor kinetics.

Herein, we present a new sodium hybrid capacitor system (NHC) that merges the merits of the quick and favorable kinetics of GNTP and GNS in an organic electrolyte with maximized energy and power densities. Employing graphene as a conductive medium in NTP promotes retention of the energy density at high current and the introduction of graphene nanosheets as an adsorption electrode significantly boosts the power density and facilitates retention of high energy. This new NHC is a promising system with exceptional features and delivers an energy density of ≈80 W h kg^{-1}, a power density of 8 kW kg^{-1}, along with lowest ever documented performance fading of ≈0.13% per 1000 cycles. This new system combines the features of a battery and a supercapacitor, establishing a trade-off relationship between them.

2. Characterization

2.1. Physical Characterization

Powder X-ray diffraction (XRD) patterns were recorded using a diffractometer (Rigaku Rint 1000, Japan) with Cu Kα radiation. Scanning electron microscopic (SEM) analysis was carried out using a field emission scanning electron microscope (Hitachi S4700, Japan). Transmission electron microscopy (TEM) images were recorded by using a Philips TecnaiF20, Holland instrument at 200 kV acceleration voltage. Raman spectra were obtained by using a Lab Ram HR-800 (Horiba, Japan) Raman dispersive spectrometer with 514.5 nm laser excitation. The graphene content in GNTP was determined by thermogravimetric analysis (TGA), using a thermal analyzer system (STA 1640, Stanton Redcroft Inc., UK). Nitrogen adsorption and desorption isotherms were recorded by using a Micromeritics ASAP 2010 surface area analyzer. X-Ray photoelectron spectroscopy (XPS) was carried out with a MultiLab 2000 (Thermo Scientific, UK) spectrometer using a monochromatized Al Kα X-ray source ($h\nu$ = 1486.71 eV).

2.2. Electrochemical Characterization

The half-cell performance was measured by using either GNTP or GNS as the working electrode and metallic sodium foil as the counter electrode. The electrode composition was as follows: 80 wt% active material, 10 wt% conductive additive (Ketjen black), and 10 wt% binder (teflonized acetylene black). The slurry was cast over a stainless steel mesh under pressure and dried at 160 °C for 4 h under vacuum prior to coin-cell fabrication. The mass loading was about 2–2.5 mg cm^{-2}. Coin-cells were assembled in a standard CR2032 configuration inside an argon-filled glove box with a moisture content of <0.1 ppm. The electrodes were separated by a porous polypropylene separator film and the electrolyte used was 1 M $NaClO_4$ in ethylene carbonate/dimethyl carbonate (1:1, v/v). A hybrid capacitor was constructed in a fashion similar to that used for the half cells after implementing a proper mass balance between the two electrodes; the test was performed under ambient conditions. Cyclic voltammetry (CV) and electrochemical impedance spectroscopy analyses were performed using a Bio-Logic electrochemical work station (SP-150, France). Galvanostatic charge–discharge studies were executed with a Won-A-Tech Battery tester (WBCS 3000, Korea) by cycling between 0 and 3 V at different current densities. The energy and power densities calculations for the hybrid capacitor are given elsewhere.[21,41,42]

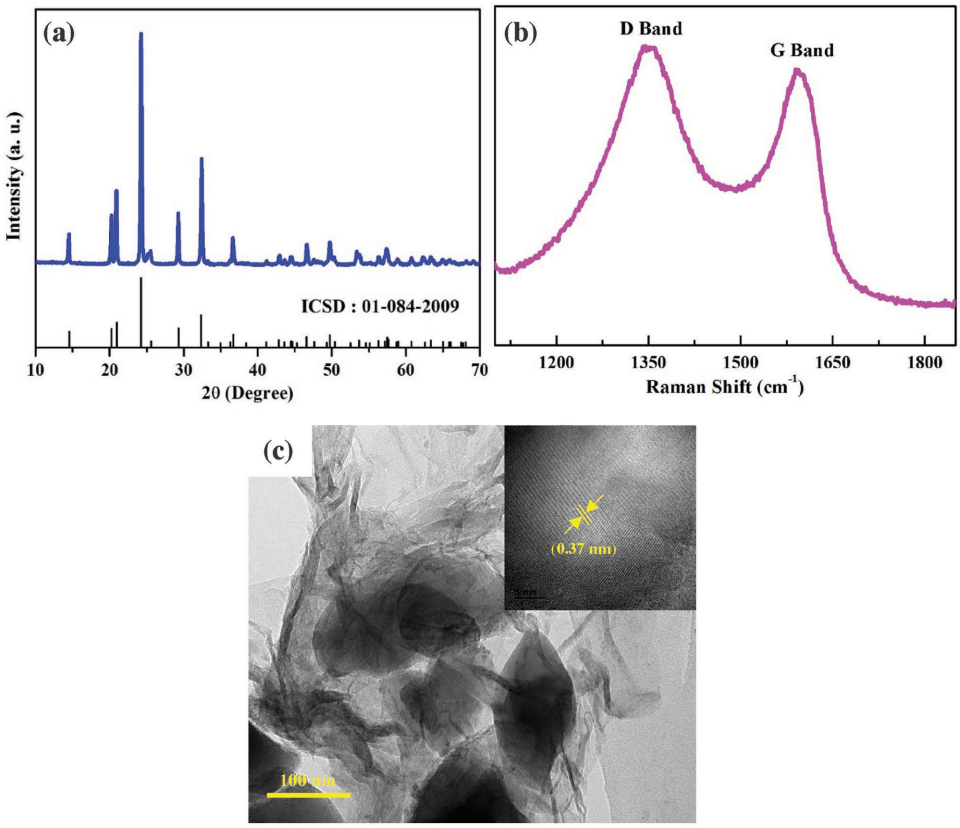

Figure 1. a) XRD pattern of GNTP, b) Raman spectrum of GNTP, c) TEM image of GNTP, inset: HRTEM image of GNTP showing the lattice fringes.

3. Results and Discussion

The XRD pattern of as-synthesized GNTP (**Figure 1**a) shows several sharp peaks, indicating the highly crystalline nature of GNTP. The observed peaks are well consistent with the reference (ICSD: 01-084-2009) and were indexed to the rhombohedral crystal structure (space group R-3m).[43,44] Typically, NTP is known for its 3D open framework, which comprises TiO_6 octahedral and PO_4 tetrahedral units in which all the corner oxygen atoms are shared, thereby providing interstitial space for Na^+ ion diffusion.[44,45] This structural arrangement enables rapid kinetics of Na^+ ions occur inside the crystal structure, leading to sodium superionic conductors.[46] The graphene content is below the detectable limit of XRD and the peaks corresponding to graphene are not visible in XRD pattern. The Raman spectrum of the GNTP particles is presented in Figure 1b, showing two strong characteristic bands at 1350 cm^{-1} (D-disordered carbon) and 1581 cm^{-1} (G-graphitic carbon), confirming the presence of graphene in the GNTP particles. The intensity ratio of the D and G bands (I_D/I_G) was about 1.05, indicating a low degree of graphitization, which is typical for reduced graphene oxide (GO) sheets.[47] The graphene content in the GNTP, quantified by TGA analysis was ≈2 wt% (Figure S1, Supporting Information) and the loss between 400 and 600 °C is attributed to graphene combustion in air. This small amount of graphene is enough to accommodate all the NTP particles due to the high surface area and 2D structure of graphene; this assists in overcoming the poor electrical conductivity of NTP and enhancing the kinetics by several orders.

The morphological features of GNTP were observed by using SEM and TEM. The SEM images in Figure S2 in the Supporting Information show that GNTP is composed of NTP particles with sizes ranging from 70 to 100 nm; these primary particles were well bridged by the graphene layers. This small particle size distribution was achieved mainly due to the presence of a graphene layer that prevented agglomeration and growth of the NTP particles during high temperature heat treatment. In addition, direct growth of the NTP particles on graphene provides an electron conducting network between NTP particles. This strategy of utilizing graphene to connect NTP particles is advantageous over utilizing other carbons since graphene exhibits the highest reported electrical conductivity and possesses a 2D structure, thereby facilitating quick and easy electron flow between the particles.[36,48]

The TEM images in Figure 1c confirmed that the NTP particles were well connected by graphene layer. Lattice fringes were clearly visible in the high-resolution TEM (HR-TEM) image, indicating the high crystallinity of the NTP particles (inset; Figure 1c). The lattice fringes with an interplanar spacing of ≈0.36 nm correspond to the (113) plane of NASICON type NTP. NASICON–NTP being with inherent high ionic conductivity, enhancing the kinetics by elevating the electronic conductivity by a highly conductive carbon network is more crucial rather than reducing their particle size, to achieve a remarkable performance in hybrid capacitors. This characteristic eliminates

the necessity of preparing much smaller nanoparticles, which has the disadvantages of low packing density and unwanted side reactions due to high surface area that could lead to poor cyclic stability.[36,49] Furthermore, the XPS survey spectrum of GNTP presented in Figure S3a in the Supporting Information confirms the presence of Na, Ti, P, and O elements in the product. The deconvoluted spectrum of Ti in Figure S3b in the Supporting Information exhibits double peaks at ≈460 and ≈465 eV, corresponding to Ti $2p_{2/3}$ and $2p_{1/2}$ peaks, confirming the tetravalent state of Ti in GNTP.[48]

A broad peak was observed at ≈24° in the XRD pattern of GNS (**Figure 2**a), corresponding to the (002) plane of amorphous graphitic carbon with a low degree of graphitization.[50] The presence of a broad peak indicates that GNS is a mixture of single- and few-layered graphene nanosheets.[51] The Raman spectrum of GNS in Figure 2b shows two characteristics peaks: (i) the G-band corresponding to the graphitic carbon layer and (ii) the D-band corresponding to significant defects or disorders in GNS.[52] The morphology of the prepared GNS was characterized by using SEM and TEM measurements. The SEM images presented in Figure S4 in the Supporting Information show a highly folded and crumpled morphology, which is typical for thermally treated graphene nanosheets. This is well-supported by the TEM images in Figure 2c, where the folded structures are more clearly visible. The formation of these folded structures is aided by the presence of oxygen defects on the graphene surface to create an intrinsically stable interior. The folded regions in the high resolution TEM image (Figure 2d) show the presence of few-layered graphene nanosheets. The chemical composition and the extent of reduction during the thermal exfoliation step were evaluated using XPS measurements. The XPS survey spectrum of GNS (Figure S5a, Supporting Information) shows the presence of carbon and oxygen in a C/O ratio of 8.87, which indicates that the oxygen functional groups were partially reduced during the thermal exfoliation step. In addition, deconvolution of the high resolution C 1s peak (Figure S5a inset, Supporting Information) shows the presence of peaks centered at 284.6, 285.5, and 286.9 eV, which can be assigned to sp^2-hybridized carbon, C—O, and C=O groups, respectively.[53] Furthermore, the surface area and pore size distribution of the prepared GNS, which play a critical role in the surface adsorption of ions, were evaluated using nitrogen adsorption/desorption isotherms. Figure S5b in the Supporting Information shows a typical type IV isotherm with a pronounced hysteresis loop, indicating the presence of mesoporous structures in the sample. The Brunaue-Emmett-Teller (BET) surface area was determined to be 435 $m^2\ g^{-1}$. This value is much lower than the theoretical specific surface area of graphene nanosheets (2630 $m^2\ g^{-1}$), which can be attributed to a reduction of the accessible surface due to partial restacking of the graphene nanosheets to a few-layered graphene.[54] Nevertheless, thermally exfoliated graphene has showed high capacitance and high affinity toward ionic adsorption in many EDLC applications due to the high accessible surface area available

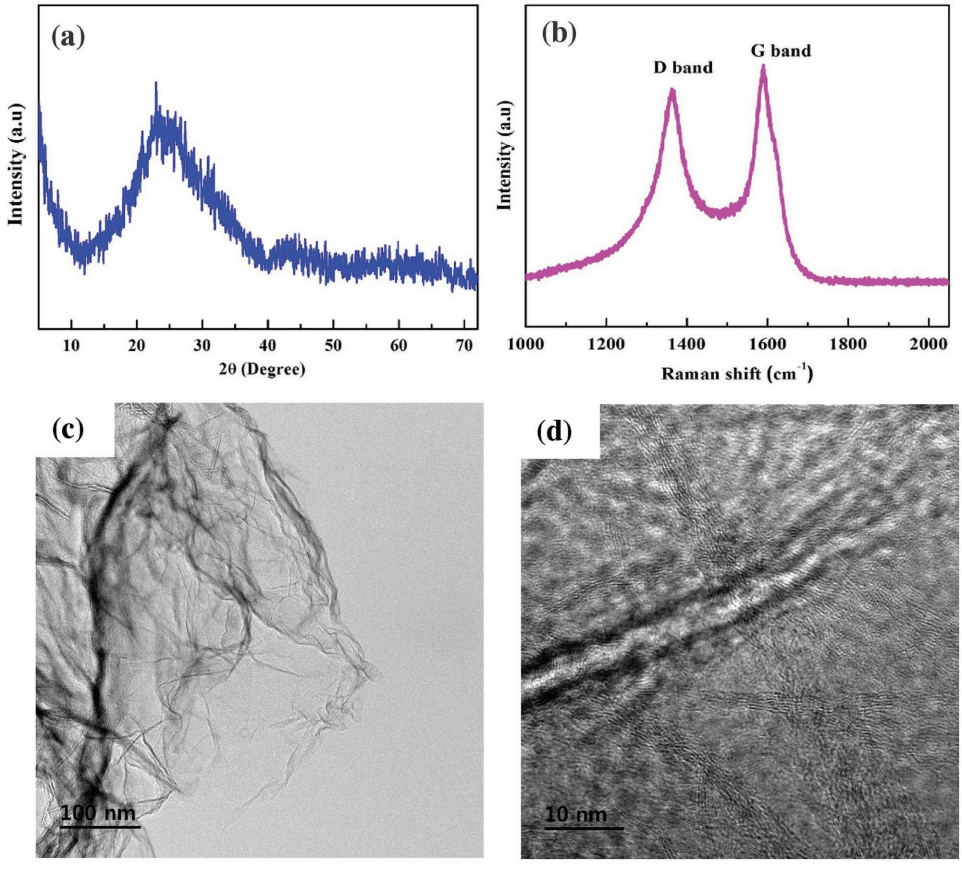

Figure 2. a) XRD pattern of GNS, b) Raman spectrum of GNS, c,d) TEM images of GNS.

for ionic adsorption.[55] Moreover, with low surface area, high packing density of active materials can be easily achieved.[56] The pore size distribution determined from the adsorption branch of the isotherm using the Barret–Joyner–Halenda method indicates the presence of mesopores with two different mean pore diameters of 2.4 and 25 nm. The presence of smaller and larger-sized mesopores provides an easily traversed ionic pathway to the electrode surface, which is critical for capacitor electrodes.[57,58]

3.1. Half-Cell Performance

The sodium ion storage capability of as-synthesized GNTP was examined in a half cell configuration by pairing against sodium foil prior to constructing a sodium hybrid capacitor. The CV curves of GNTP were measured in the potential range of 0.01–3 V versus Na/Na^+ at a sweep rate of 0.1 mV s^{-1}, as presented in Figure S6a in the Supporting Information. During the cathodic scan, a broad irreversible peak was observed in the range of 1.08–0.4 V in the first cycle, which disappeared in the subsequent cycle. This irreversible reductive current is attributed to the formation of an SEI layer and electrolyte decomposition.[34,59,60] Further, two main redox peaks were observed at ≈2.07 and ≈0.33 V, which are attributed to the redox reactions of the Ti^{4+}/Ti^{3+} and Ti^{3+}/Ti^{2+} couples, respectively. The reversible sodium extraction that occurred around ≈0.5 and ≈2.25 V corresponded to the Ti^{2+}/Ti^{3+} and Ti^{3+}/Ti^{4+} redox reactions, respectively.[34,59,60] Traditionally, titanium-based electrodes utilize the redox reaction of Ti^{4+}/Ti^{3+} to insert sodium ions. However, when the potential range was extended to 0.01 V, a new redox reaction of Ti^{3+}/Ti^{2+} was achieved, thereby allowing insertion of more sodium ions at a relatively low potential.[33,60–62] The possibility of insertion of more sodium ions by titanium-based electrodes, such as $Na_2Ti_3O_7$ and $Na_3Ti_2(PO_4)_3$, via the new redox pathway was also demonstrated in previous literature.[34,59,60]

Figure 3a shows the constant current charge–discharge curves of GNTP at the current density of 250 mA g^{-1}. The discharge curves of GNTP displayed two working plateaus; the first is the usual plateau at ≈2.07 V for the Ti^{4+}/Ti^{3+} redox couple inserting two sodium ions, and the second is a new plateau around ≈0.33 V due to the Ti^{3+}/Ti^{2+} redox couple, confirming the insertion of extra sodium ions.[33,59,60] During charging, the profile of GNTP showed plateaus around ≈0.44 and ≈2.2 V, with titanium returning to its tetravalent state.[63] These results are highly consistent with the CV results. Although GNTP delivered a low initial Columbic efficiency due to formation of the SEI layer during the first cycle, the Columbic efficiency improved and stabilized around 98% with cycling. Similarly, the discharge capacity declined in the initial few cycles and stabilized at the seventh cycle with a discharge capacity of ≈157 mA h g^{-1}.[21,33] After 150 cycles, GNTP delivered a discharge capacity of 145 mA h g^{-1} and retained almost 90% of the capacity from the seventh cycle (Figure 3b). This demonstrates the highly stable nature of GNTP even at low voltage, which is mainly attributed to the NASICON structure with a strong inductive effect from the PO_4 tetrahedra.[33,60] GNTP demonstrated an excellent rate performance by delivering a specific capacity of ≈200, 141, 98, 69 mA h g^{-1} at 0.1, 0.5, 2, 3.2 A g^{-1}, respectively (Figure S6b, Supporting Information), depicting the ability of GNTP to store Na ions at high power condition. The graphene layers acted as a buffer to prevent the occurrence of volume expansion at lower voltage due to the insertion of extra sodium ions. In addition, the graphene layers enhanced the electrical conductivity and

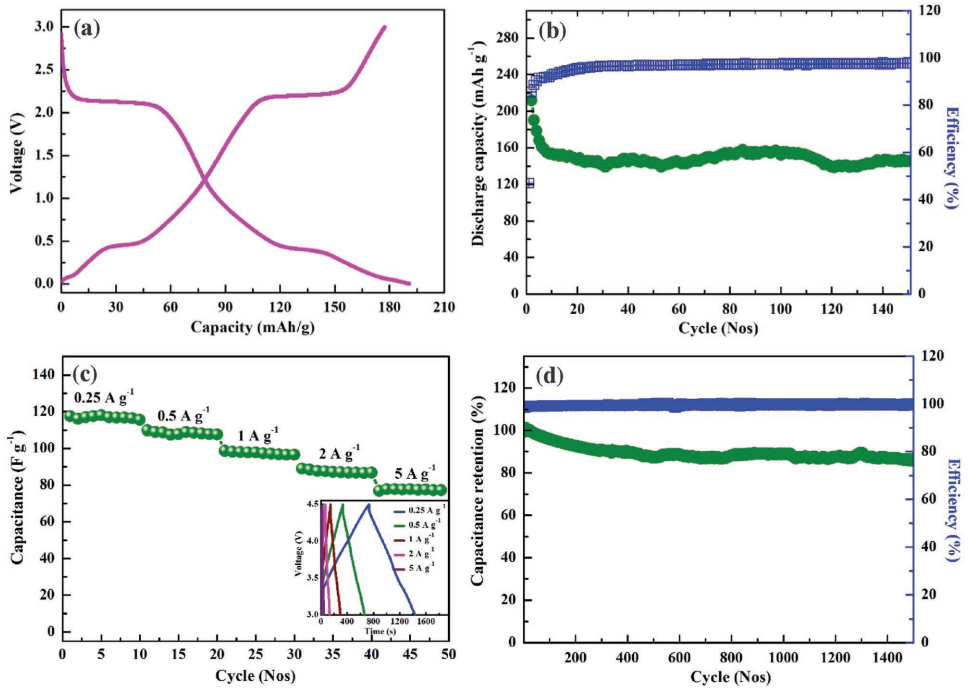

Figure 3. a) Charge–discharge profile of GNTP versus Na in the range of 0.01–3 V, b) cyclic stability of GNTP, c) rate performance of GNS versus Na in the range of 3–4.5 V; Inset: charge–discharge profiles of GNS versus Na, d) cyclic stability of GNS.

facilitated easy diffusion of sodium ions into the NTP particles.[58] With these enhanced properties, GNTP is expected to be a superior insertion electrode for NHCs.

The electrochemical performance of GNS was analyzed in the potential range of 3–4.5 V using a half cell configuration by coupling with metallic sodium. The CV curves of GNS (Figure S7, Supporting Information) have a perfectly rectangular-box shape, indicating the typical capacitive behavior of GNS due to double layer formation.[21,23] With increasing scan rate, the rectangular shape was retained without any distortions, indicating quick ion adsorption kinetics because of the superior electronic conductivity of GNS and the easy access of ions to the interface. Within this potential window, no intercalation or electrolyte decomposition was observed and the working mechanism can be purely attributed to reversible ClO_4 anion adsorption/desorption on the surface.[25,64,65] This is well supported by the charge–discharge voltage profiles (Figure 3c), which are highly linear with triangular shape profile, accounting to a capacitance of ≈99 F g^{-1} at the current density of 1 A g^{-1}. There are no deviations or visible humps in the curves, indicating facile surface adsorption behavior of the GNS electrodes.[42,43] The obtained capacitance is attributed only due to ClO_4^- adsorption, thereby eliminating the contribution from pseudocapacitance from functional groups which could reduce the cyclability of GNS electrodes.[66] The obtained capacitance is one the highest ever achieved for an adsorption electrode, given that activated carbon-type electrodes deliver a limited capacitance of around 65–80 F g^{-1} at this current density and fails at higher current density.[26,38,67–69] GNS retained a high capacitance of ≈118, 107, 88, and 78 F g^{-1} at the corresponding current densities of 0.25, 0.5, 2, and 5 A g^{-1} (Figure 3c). Moreover, the GNS electrode retained ≈86% of its initial capacitance even after 1500 cycles at 1 A g^{-1} (Figure 3d). The initial capacitance loss during cycling could be attributed due to degradation of surface functionalities.[25] This demonstrates the highly reversible adsorption/desorption characteristics of graphene, making it an attractive high power adsorption electrode for the next-generation NHCs. Despite the low surface area relative to the theoretical surface area, this high performance is attributed to the high electronic conductivity and the complete accessibility of the surface to the ions even at higher currents.[70] This is specifically facilitated by the presence of a large number of individual graphene sheets and the large number of mesopores in GNS, providing quicker channels for ion adsorption at high current. Also, the higher electronic conductivity of GNS relative to that of conventional ACs increases the affinity of GNS toward ion adsorption.[71] GNS is a highly attractive and promising adsorption electrode for sodium capacitors than ACs, porous carbon derived from various precursors, and carbon nano tubes (CNTs).

3.2. Hybrid Capacitor

To exploit the advantages of the high performing GNTP and GNS electrodes, an NHC was constructed by coupling the electrodes and utilizing an organic electrolyte to maximize the energy density of the system. The mass balance was set at 1:3 and the performance of the NHC was analyzed via CV and galvanostatic charge–discharge (GCD) measurements between 0 and 3 V. The CV curve of NHC presented in Figure S8 in the Supporting Information is not a perfect rectangle as in the case of an EDLC, but is irregular, comprising a combination of a rectangular region and redox peaks. The redox peaks are clearly visible, and can be attributed to the intercalation/deintercalation of Na^+ ions into GNTP, while the broad rectangular region is due to the adsorption/desorption of anions over GNS.[21,25,72] The former confirms the battery behavior and the latter confirms the capacitor behavior, thereby making this system a hybrid one.[73,74] Based on this result, the reaction mechanism of NHC is proposed as follows: (i) during charging, Na^+ ions are intercalated into GNTP by a redox reaction, creating a charge imbalance in the system. To alleviate this charge imbalance, ClO_4^- anions are quickly adsorbed on GNS to form a double layer and stabilize the system. (ii) During discharge, Na^+ ions are deintercalated from GNTP, and simultaneously, ClO_4^- anions are desorbed from the surface of GNS. This working principle of the NHC is represented in **Scheme 1**.

The reversible two sodium ions intake per unit cell through Ti^{4+}/Ti^{3+} redox is favorable for achieving high energy density. The charge–discharge curves of NHC in **Figure 4**a are neither linear nor triangular in shape, reconfirming the results of the CV studies, indicating a dual charge storage mechanism in the hybrid capacitor. The GCD curves were a fusion of a plateau due to Na^+ ion intercalation/deintercalation by the Ti redox reaction and a sloppy curve due to anionic adsorption/desorption over GNS. Even at higher currents, the GCD curves of the NHC retained its unique shape, indicating facile sodium intercalation/deintercalation inside GNTP, along with quick adsorption and desorption over GNS. The present kinetically enhanced system is compared with traditional hybrid capacitors in Figure S9 in the Supporting Information. The superior performance of NHC was largely due to the enhanced electrical conductivity of GNTP, having high capacity for insertion of more sodium ions, allowing the reaction to proceed smoothly even under severe conditions.[72] The electrical conductivity of small NTP particles that are trapped between graphene layers is greatly increased, thereby providing a space for the electrochemical reaction to occur without difficulty.[36,47] Moreover, the fast sodium kinetics of NTP facilitates quick insertion of sodium ions into the tunnel-like structures. The pores in GNS

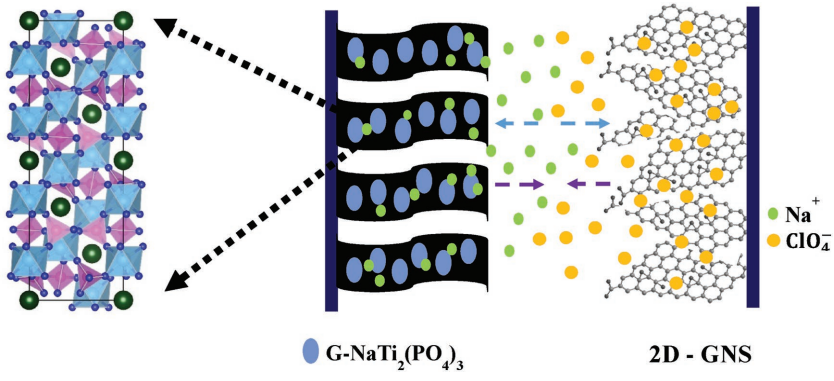

Scheme 1. Operating mechanism of NHC.

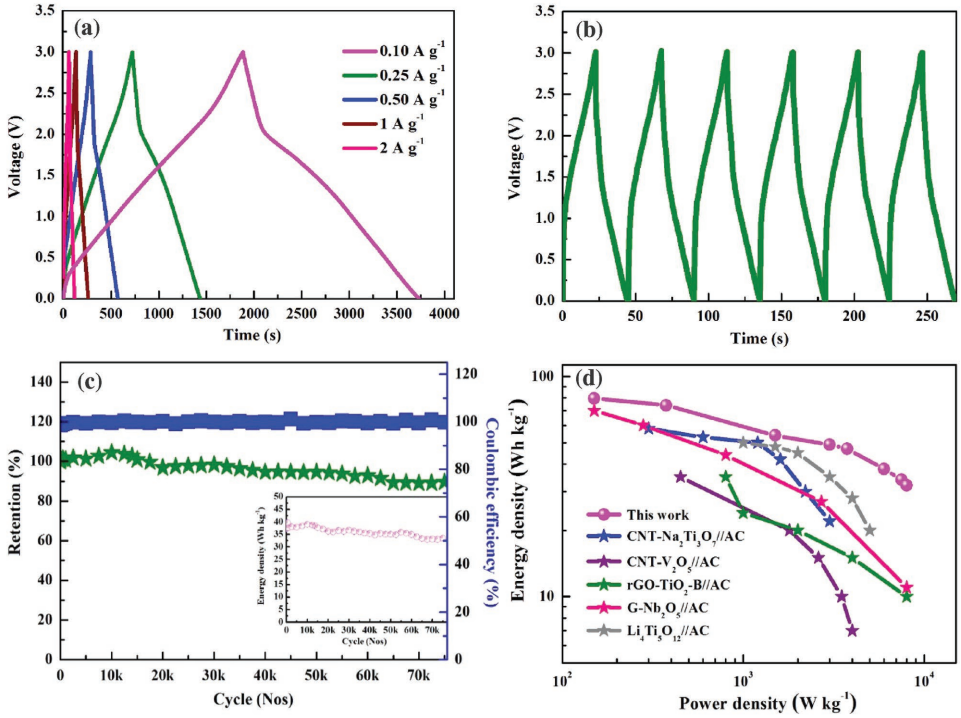

Figure 4. a) Charge–discharge curves of NHC at different current densities, b) charge–discharge curves of NHC at 4 A g^{-1}, c) cyclic stability of NHC at 4 A g^{-1}. Inset: corresponding energy density. d) Ragone plot of NHC and comparison with other hybrid capacitor systems.

further store electrolyte and provide ions for easy adsorption, and the functional groups on the graphene surface help to reduce the interfacial resistance, allowing the ions to approach the surface quickly.[75] Traditional hybrid capacitor system fails to achieve this remarkable energy output at high power due to kinetic imbalance between the carbon coated intercalation compound and activated carbon electrodes at high current. At high current rate, sodium intercalation and anionic adsorption becomes almost negligible due to high resistance in low conductive porous carbon.

Longevity is an important characteristic of any energy storage system that must be imparted to hybrid systems to make them more commercially viable. Therefore, the long term performance of the NHC was evaluated at high current density of 4 A g^{-1} (Figure 4b). The NHC underwent very little performance degradation even after 75 000 charge–discharge cycles, with retention of 90% of the initial performance with near 100% coulombic efficiency (Figure 4c). Unlike the behavior documented in previous reports and conventional hybrid capacitors that show noticeable performance degradation even within 1000 cycles, the newly developed system exhibited an ultralow performance fading of ≈0.13% per 1000 cycles. This is the lowest documented performance degradation ever achieved for hybrid capacitors, obtained even with a large voltage window of 0–3 V; the previous reports used narrow voltage windows to achieve good stability.[23,25,38,76] This is owing to the robust structural stability of the NASICON framework, which can withstand the harsh sodium insertion/extraction process, and the presence of graphene nanosheets that can buffer the any volume changes during additional sodium ion insertion into the structure and also reducing interfacial charge transfer resistance.[21]

The significantly enhanced performance of this new system was further demonstrated by constructing the Ragone plot and comparing it with data from other reports (Figure 4d). The Ragone plot clearly shows that NHC retained much higher specific energy at high power than those of hybrid capacitor systems utilizing AC or CNTs as adsorption electrodes where energy loss at high power is very high. The energy density obtained is highly competitive with and comparable to that of modern rechargeable batteries, while the specific power achieved is equivalent to that of EDLCs. With its ultrastability and durability, the NHC delivered a specific energy of ≈34 W h kg^{-1} after 75 000 cycles, accounting to a loss of ≈0.13% of its initial energy density per 1000 cycles (Figure 4b Inset). With this superior energy retention at high power along with ultradurability, this new NHC could be an efficient candidate to power electric and hybrid electric vehicles easily. Further, the NHC performance is the highest ever reported and surpasses all previously documented hybrid capacitors (both sodium and lithium) that employ intercalation-based electrodes intercalation and pseudocapacitance-based capacitor systems, such as AC//$LiCoO_2$, AC//$LiMn_2O_4$, CNT//TiO_2-B, AC//MnO_2, G-Fe_2O_3 //3D-Graphene, AC//V_2O_5, rGO-Nb_2O_5//AC, Li_2MnSiO_4//AC, and especially commercial lithium hybrid capacitors that utilize AC//graphite and AC//$Li_4Ti_5O_{12}$; the performance even surpasses that of the recently reported high-performing sodium hybrid capacitors (**Figure 5**a).[24,26,38,42,46,72,77,78] Moreover, we recently reported a high energy sodium hybrid capacitor beyond lithium, but these new results far outweigh those of the reported system, especially in terms of power density and cyclability. The specific energy and specific power obtained herein are compared to those of other reported systems in

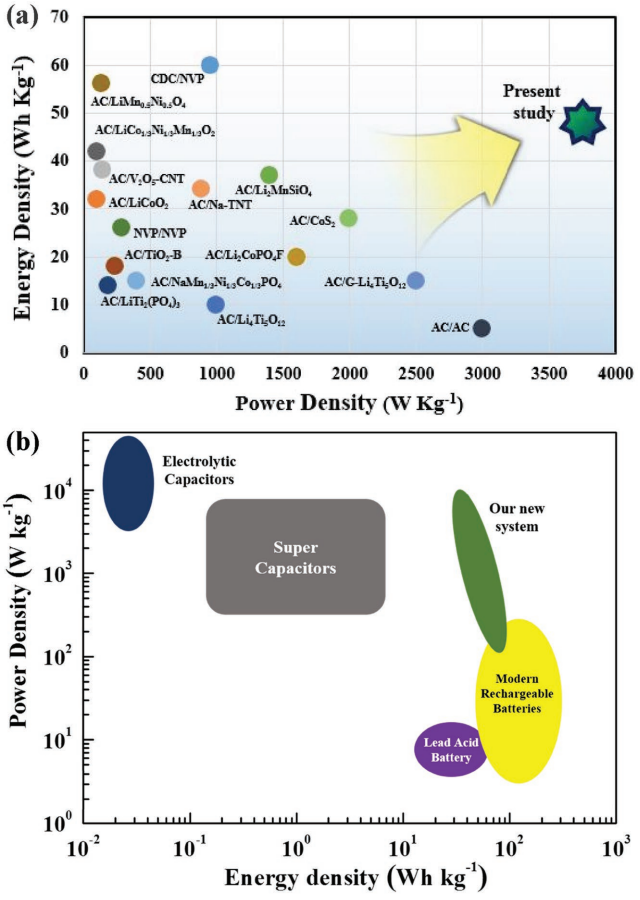

Figure 5. a) Comparison of performance of NHC with other hybrid capacitor systems, b) Ragone plot of NHC compared with commercial energy storage devices.

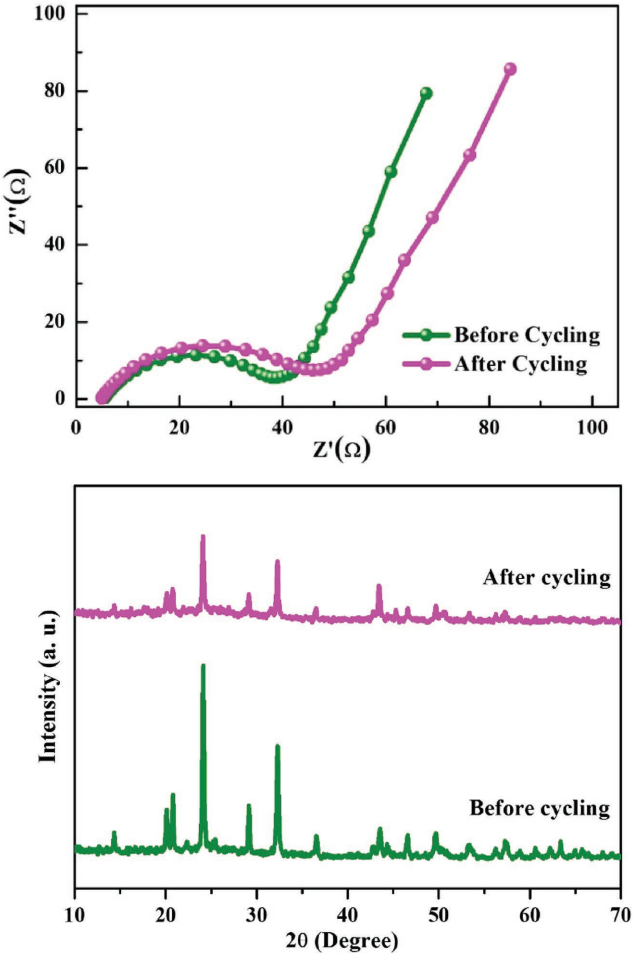

Figure 6. a) Nyquist plots of NHC: before and after cycling, b) ex situ XRD patterns of GNTP before and after cycling in NHC.

Figure 5a and Table S1 in the Supporting Information. Additionally, the stability of this novel NHC surpassed the previously reported sodium ion capacitors, where energy loss per cycle is really high and thereby making it a competitive energy storage system.[24,25,79–81] The performance of the NHC is further compared with other commercial energy storage systems by a Ragone plot, as presented in Figure 5b, it surpassed performance of lead acid batteries and highly competitive with that of modern rechargeable batteries and capacitors. NHC retains more specific energy even at high specific powers where batteries and capacitors fail to work efficiently. Further, the performance of the NHC meets the requirements for the next-generation energy storage systems to power hybrid vehicles and also makes it a promising candidate for large-scale grid storage applications.

To elucidate the origin of this superior performance, Nyquist plots (**Figure 6**a) were recorded before and after prolonged cycling. The Nyquist plots had a perfectly semicircular profile in the high frequency region due to the charge transfer reaction at the electrode–electrolyte interface and an inclined line in the low frequency range due to sodium insertion and extraction.[82] A slight reduction in the solution resistance was noted after prolonged cycling and no obvious change in the charge transfer resistance was noted, indicating that the surface is still highly active and available for sodium ion intercalation. Furthermore, CV traces were recorded after cycling and no apparent change in the shape of the curves was noted (Figure S10, Supporting Information). The redox peaks were clearly visible even after 75 000 robust cycles, indicating that GNTP was still highly active and readily available for sodium insertion. The only change noted was a slight reduction in the area under the CV curve. The XRD patterns of GNTP after cycling in NHC is presented in Figure 6b and it still maintains the crystallinity along with all major NASICON peaks, with zero-strain characteristics. It implies that the structural integrity of GNTP particles is well preserved even after harsh cycling and still available for reaction.

The superior performance of this new NHC system is attributed to: (i) utilization of the NASICON-structured GNTP that facilitated easy and quick insertion of sodium ions into battery electrode and favorably enhanced the energy density, (ii) the graphene in GNTP enhanced the electronic conductivity by many orders and reduced the Na^+ diffusion path-length, thereby enabling fast transport of Na^+ ions, (iii) choice of highly conductive, few-layered graphene nanosheets as an adsorption electrode, the adsorption kinetics of which is far superior to that of ACs, providing a large number of pores for adsorption even at high current rates, (iv) the presence of mesopores in

GNS provides a favorable path for ions to move easily inside GNS and to form a double layer in a facile manner, (v) the inherent stable nature of NASICON structured NTP overcome any volume expansion during the reaction and maintained the stability for prolonged cycles, (vi) the surfaces of both electrodes are highly conductive, thereby reducing interfacial and charge transfer resistance to a greater extent and favoring to achieve a high specific energy at high specific power.

4. Conclusion

In summary, we have demonstrated an effective and simple strategy for improving the performance of sodium hybrid capacitors by utilizing a graphene-aided, structurally stable $NaTi_2(PO_4)_3$ intercalation electrode with faster reaction kinetics and GNS adsorption electrode. The strategy of utilizing graphene in both electrodes prevents the specific energy loss at high power and thus the NHC performed efficiently even at a high power of 8 kW kg^{-1} without specific energy loss. Moreover, NHC was stable for 75 000 cycles with an ultralow performance fading rate of ≈0.13% per 1000 cycles, which is the lowest ever reported for a hybrid capacitor. Such superior performance was made possible by enhancing the electrical conductivity and balancing the reaction kinetics between the intercalation and adsorption electrodes in the hybrid system, resulting in higher power and higher energy than state-of-the-art batteries and capacitors. The obtained performance are high enough to meet the demands of advanced energy storage systems, which could pave the way for further exploration of graphene utilization in the next-generation hybrid capacitor systems to retain a large energy density even at a high specific power.

5. Experimental Section

GO solution was prepared from natural graphite flakes by a well-known modified Hummer's, method, and an aqueous GO dispersion was used for preparation of GNTP.[83] For the preparation of GNTP, a certain amount of GO was dispersed in a mixture of distilled water and ethanol with ultrasonication for 1 h. A stoichiometric amount of titanium butoxide $[Ti(C_4H_9O)_4]$ was then added to the above solution, leading to formation of titanyl hydroxide under constant stirring. Nitric acid solution was added dropwise to the above solution mixture to convert titanyl hydroxide into titanyl nitrate $[Ti(NO_3)_2]$. A stoichiometric amount of Na_2CO_3 and $NH_4H_2PO_4$ was added to the above solution and was well sonicated for homogenous mixing. The solvent was evaporated and a gelled precursor was obtained after drying the mixture. Finally, the precursor was well ground and subjected to preheat treatment at 350 °C for 3 h, followed by final calcination at 700 °C for 10 h under argon atmosphere. The obtained GNTP products were further characterized. GNS was prepared by thermal exfoliation of graphite oxide (obtained using the modified Hummer's method) under nitrogen atmosphere at 700 °C, where ultrasonication was employed prior to the thermal exfoliation step. The ultrasonication step was adopted to prevent splashing of the sample due to the huge volume change that occurs during exfoliation.

Supporting Information

Supporting Information is available from the Wiley Online Library or from the author.

Acknowledgements

R.T. and B.M. contributed equally to this work. This work was supported by the National Research Foundation of Korea (NRF) grant funded by the Korea government (Ministry of Science, ICT and Future Planning) (No. 2016R1A4A1012224). D.K. Kim acknowledges the support from the Climate Change Research Hub of KAIST (Grant No. N11160019).

Received: December 9, 2016
Revised: January 17, 2017
Published online:

[1] K. Kang, Y. S. Meng, J. Bréger, C. P. Grey, G. Ceder, *Science* **2006**, *311*, 977.
[2] P. G. Bruce, S. A. Freunberger, L. J. Hardwick, J.-M. Tarascon, *Nat. Mater.* **2012**, *11*, 19.
[3] M. Armand, J. M. Tarascon, *Nature* **2008**, *451*, 652.
[4] B. Scrosati, J. Hassoun, Y.-K. Sun, *Energy Environ. Sci.* **2011**, *4*, 3287.
[5] M. D. Slater, D. Kim, E. Lee, C. S. Johnson, *Adv. Funct. Mater.* **2013**, *23*, 947.
[6] C. Liu, F. Li, L.-P. Ma, H.-M. Cheng, *Adv. Mater.* **2010**, *22*, E28.
[7] H. Jiang, P. S. Lee, C. Li, *Energy Environ. Sci.* **2013**, *6*, 41.
[8] J. M. Tarascon, M. Armand, *Nature* **2001**, *414*, 359.
[9] S.-W. Kim, D.-H. Seo, X. Ma, G. Ceder, K. Kang, *Adv. Energy Mater.* **2012**, *2*, 710.
[10] B. L. Ellis, L. F. Nazar, *Curr. Opin. Solid State Mater. Sci.* **2012**, *16*, 168.
[11] D. Kundu, E. Talaie, V. Duffort, L. F. Nazar, *Angew. Chem., Int. Ed.* **2015**, *54*, 3431.
[12] M. Dahbi, N. Yabuuchi, K. Kubota, K. Tokiwa, S. Komaba, *Phys. Chem. Chem. Phys.* **2014**, *16*, 15007.
[13] J. Wang, S. Kaskel, *J. Mater. Chem.* **2012**, *22*, 23710.
[14] Y. Xu, Z. Lin, X. Zhong, X. Huang, N. O. Weiss, Y. Huang, X. Duan, *Nat. Commun.* **2014**, *5*, 4554.
[15] J. R. Miller, P. Simon, *Science* **2008**, *321*, 651.
[16] Y. Zhai, Y. Dou, D. Zhao, P. F. Fulvio, R. T. Mayes, S. Dai, *Adv. Mater.* **2011**, *23*, 4828.
[17] K. Karthikeyan, S. Amaresh, S. N. Lee, X. Sun, V. Aravindan, Y.-G. Lee, Y. S. Lee, *ChemsusChem* **2014**, *7*, 1435.
[18] J. B. Cook, H.-S. Kim, T. C. Lin, C.-H. Lai, B. Dunn, S. H. Tolbert, *Adv. Energy Mater.* **2016**, *7*, 1601283.
[19] B. Li, F. Dai, Q. Xiao, L. Yang, J. Shen, C. Zhang, M. Cai, *Adv. Energy Mater.* **2016**, *6*, 1600802.
[20] D. P. Dubal, O. Ayyad, V. Ruiz, P. Gomez-Romero, *Chem. Soc. Rev.* **2015**, *44*, 1777.
[21] R. Thangavel, K. Kaliyappan, K. Kang, X. Sun, Y.-S. Lee, *Adv. Energy Mater.* **2016**, *6*, 1502199.
[22] V. Aravindan, J. Gnanaraj, Y.-S. Lee, S. Madhavi, *Chem. Rev.* **2014**, *114*, 11619.
[23] H. Wang, D. Mitlin, J. Ding, Z. Li, K. Cui, *J. Mater. Chem. A* **2016**, *4*, 5149
[24] R. Wang, J. Lang, P. Zhang, Z. Lin, X. Yan, *Adv. Funct. Mater.* **2015**, *25*, 2270.
[25] J. Ding, H. Wang, Z. Li, K. Cui, D. Karpuzov, X. Tan, A. Kohandehghan, D. Mitlin, *Energy Environ. Sci.* **2015**, *8*, 941.
[26] K. Karthikeyan, S. Amaresh, K. J. Kim, S. H. Kim, K. Y. Chung, B. W. Cho, Y. S. Lee, *Nanoscale* **2013**, *5*, 5958.
[27] Y. Wen, K. He, Y. Zhu, F. Han, Y. Xu, I. Matsuda, Y. Ishii, J. Cumings, C. Wang, *Nat. Commun.* **2014**, *5*, 4033
[28] K. Chihara, A. Kitajou, I. D. Gocheva, S. Okada, J.-i. Yamaki, *J. Power Sources* **2013**, *227*, 80.
[29] H. Kim, H. Kim, Z. Ding, M. H. Lee, K. Lim, G. Yoon, K. Kang, *Adv. Energy Mater.* **2016**, *6*, 1600943.

[30] K. Saravanan, C. W. Mason, A. Rudola, K. H. Wong, P. Balaya, *Adv. Energy Mater.* **2013**, *3*, 444.
[31] Y. Fang, L. Xiao, J. Qian, Y. Cao, X. Ai, Y. Huang, H. Yang, *Adv. Energy Mater.* **2016**, *6*, 1502197.
[32] S. Li, Y. Dong, L. Xu, X. Xu, L. He, L. Mai, *Adv. Mater.* **2014**, *26*, 3545.
[33] D. Wang, Q. Liu, C. Chen, M. Li, X. Meng, X. Bie, Y. Wei, Y. Huang, F. Du, C. Wang, G. Chen, *ACS Appl. Mater. Interfaces* **2016**, *8*, 2238.
[34] G. Pang, C. Yuan, P. Nie, B. Ding, J. Zhu, X. Zhang, *Nanoscale* **2014**, *6*, 6328.
[35] Y. H. Jung, C. H. Lim, D. K. Kim, *J. Mater. Chem. A* **2013**, *1*, 11350.
[36] C. H. Lim, A. G. Kannan, H.-W. Lee, D. K. Kim, *J. Mater. Chem. A* **2013**, *1*, 6183.
[37] K. Naoi, S. Ishimoto, J.-i. Miyamoto, W. Naoi, *Energy Environ. Sci.* **2012**, *5*, 9363.
[38] H. Kim, M.-Y. Cho, M.-H. Kim, K.-Y. Park, H. Gwon, Y. Lee, K. C. Roh, K. Kang, *Adv. Energy Mater.* **2013**, *3*, 1500.
[39] E. Frackowiak, F. Béguin, *Carbon* **2001**, *39*, 937.
[40] L. L. Zhang, X. S. Zhao, *Chem. Soc. Rev.* **2009**, *38*, 2520.
[41] K. Karthikeyan, S. Amaresh, S. N. Lee, V. Aravindan, Y. S. Lee, *Chem.—Asian J.* **2014**, *9*, 852.
[42] K. Kaliyappan, S. Amaresh, Y.-S. Lee, *ACS Appl. Mater. Interfaces* **2014**, *6*, 11357.
[43] S. I. Park, I. Gocheva, S. Okada, J.-i. Yamaki, *J. Electrochem. Soc.* **2011**, *158*, A1067.
[44] C. Delmas, A. Nadiri, J. L. Soubeyroux, *Solid State Ionics* **1988**, *28–30*, 419.
[45] Z. Li, D. Young, K. Xiang, W. C. Carter, Y.-M. Chiang, *Adv. Energy Mater.* **2013**, *3*, 290.
[46] H. Du, H. Yang, C. Huang, J. He, H. Liu, Y. Li, *Nano Energy* **2016**, *22*, 615.
[47] A. C. Ferrari, J. C. Meyer, V. Scardaci, C. Casiraghi, M. Lazzeri, F. Mauri, S. Piscanec, D. Jiang, K. S. Novoselov, S. Roth, A. K. Geim, *Phys. Rev. Lett.* **2006**, *97*, 187401.
[48] C. Wu, P. Kopold, Y.-L. Ding, P. A. van Aken, J. Maier, Y. Yu, *ACS Nano* **2015**, *9*, 6610.
[49] M. Pumera, *Energy Environ. Sci.* **2011**, *4*, 668.
[50] H. Yang, S. Kannappan, A. S. Pandian, J.-H. Jang, Y. S. Lee, W. Lu, *J. Power Sources* **2015**, *284*, 146.
[51] V. Chabot, D. Higgins, A. Yu, X. Xiao, Z. Chen, J. Zhang, *Energy Environ. Sci.* **2014**, *7*, 1564.
[52] K. N. Kudin, B. Ozbas, H. C. Schniepp, R. K. Prud'homme, I. A. Aksay, R. Car, *Nano Lett.* **2008**, *8*, 36.
[53] R. Karthick, M. Brindha, M. Selvaraj, S. Ramu, *J. Colloid Interface Sci.* **2013**, *406*, 69.
[54] H.-B. Zhang, J.-W. Wang, Q. Yan, W.-G. Zheng, C. Chen, Z.-Z. Yu, *J. Mater. Chem.* **2011**, *21*, 5392.
[55] M. D. Stoller, C. W. Magnuson, Y. Zhu, S. Murali, J. W. Suk, R. Piner, R. S. Ruoff, *Energy Environ. Sci.* **2011**, *4*, 4685.
[56] M. D. Stoller, S. Park, Y. Zhu, J. An, R. S. Ruoff, *Nano Lett.* **2008**, *8*, 3498.
[57] D. R. Dreyer, S. Park, C. W. Bielawski, R. S. Ruoff, *Chem. Soc. Rev.* **2010**, *39*, 228.
[58] Y. Sun, Q. Wu, G. Shi, *Energy Environ. Sci.* **2011**, *4*, 1113.
[59] Y. Niu, M. Xu, C. Guo, C. M. Li, *J. Alloys Compd.* **2016**, *474*, 88.
[60] P. Senguttuvan, G. Rousse, M. E. Arroyo y de Dompablo, H. Vezin, J. M. Tarascon, M. R. Palacín, *J. Am. Chem. Soc.* **2013**, *135*, 3897.
[61] Y. Kim, K.-s. Park, S.-h. Song, J. Han, J. B. Goodenough, *J. Electrochem. Soc.* **2009**, *156*, A703.
[62] P. Senguttuvan, G. Rousse, V. Seznec, J.-M. Tarascon, M. R. Palacín, *Chem. Mater.* **2011**, *23*, 4109.
[63] J. Yang, H. Wang, P. Hu, J. Qi, L. Guo, L. Wang, *Small* **2015**, *11*, 3744.
[64] H. Li, L. Peng, Y. Zhu, X. Zhang, G. Yu, *Nano Lett.* **2016**, *16*, 5938.
[65] H. Li, Y. Zhu, S. Dong, L. Shen, Z. Chen, X. Zhang, G. Yu, *Chem. Mater.* **2016**, *28*, 5753.
[66] L. Wei, M. Sevilla, A. B. Fuertes, R. Mokaya, G. Yushin, *Adv. Funct. Mater.* **2012**, *22*, 827.
[67] M. Biswal, A. Banerjee, M. Deo, S. Ogale, *Energy Environ. Sci.* **2013**, *6*, 1249.
[68] K. Karthikeyan, S. Amaresh, S.-N. Lee, J.-Y. An, Y.-S. Lee, *ChemsusChem* **2014**, *7*, 2310.
[69] E. Lim, C. Jo, M. S. Kim, M.-H. Kim, J. Chun, H. Kim, J. Park, K. C. Roh, K. Kang, S. Yoon, J. Lee, *Adv. Funct. Mater.* **2016**, *26*, 3711.
[70] L. Eliad, E. Pollak, N. Levy, G. Salitra, A. Soffer, D. Aurbach, *Appl. Phys. A* **2005**, *82*, 607.
[71] D. Lozano-Castelló, D. Cazorla-Amorós, A. Linares-Solano, S. Shiraishi, H. Kurihara, A. Oya, *Carbon* **2003**, *41*, 1765.
[72] E. Lim, C. Jo, H. Kim, M.-H. Kim, Y. Mun, J. Chun, Y. Ye, J. Hwang, K.-S. Ha, K. C. Roh, K. Kang, S. Yoon, J. Lee, *ACS Nano* **2015**, *9*, 7497.
[73] H. Wang, C. Guan, X. Wang, H. J. Fan, *Small* **2015**, *11*, 1470.
[74] F. Wang, X. Wang, Z. Chang, X. Wu, X. Liu, L. Fu, Y. Zhu, Y. Wu, W. Huang, *Adv. Mater.* **2015**, *27*, 6962.
[75] S. Amaresh, K. Karthikeyan, I. C. Jang, Y. S. Lee, *J. Mater. Chem. A* **2014**, *2*, 11099.
[76] J. Yin, L. Qi, H. Wang, *ACS Appl. Mater. Interfaces* **2012**, *4*, 2762.
[77] E. Lim, H. Kim, C. Jo, J. Chun, K. Ku, S. Kim, H. I. Lee, I.-S. Nam, S. Yoon, K. Kang, J. Lee, *ACS Nano* **2014**, *8*, 8968.
[78] H. Kim, K.-Y. Park, J. Hong, K. Kang, *Sci. Rep.* **2014**, *4*, 5278.
[79] H. Wang, Y. Zhang, H. Ang, Y. Zhang, H. T. Tan, Y. Zhang, Y. Guo, J. B. Franklin, X. L. Wu, M. Srinivasan, H. J. Fan, Q. Yan, *Adv. Funct. Mater.* **2016**, *26*, 3082.
[80] Y. Zhao, L. Hu, S. Zhao, L. Wu, *Adv. Funct. Mater.* **2016**, *26*, 4038.
[81] R. Yi, S. Chen, J. Song, M. L. Gordin, A. Manivannan, D. Wang, *Adv. Funct. Mater.* **2014**, *24*, 7433.
[82] K. Karthikeyan, V. Aravindan, S. B. Lee, I. C. Jang, H. H. Lim, G. J. Park, M. Yoshio, Y. S. Lee, *J. Power Sources* **2010**, *195*, 3761.
[83] W. S. Hummers, R. E. Offeman, *J. Am. Chem. Soc.* **1958**, *80*, 1339.